A Finite Temperature Multiscale Interphase Zone Model and Simulations of Fracture

Lisheng Liu
Department of Civil and Environmental Engineering, The University of California, Berkeley, CA 94720; Department of Engineering Structure and Mechanics, Wuhan University of Technology, Wuhan, 430070, P.R. China

Shaofan Li[1]
Department of Civil and Environmental Engineering, The University of California, Berkeley, CA 94720
e-mail: shaofan@berkeley.edu

In this work, an atomistic-based finite temperature multiscale interphase finite element method has been developed, and it has been applied to study fracture process of metallic materials at finite temperature. The coupled thermomechanical finite element formulation is derived based on continuum thermodynamics principles. The mesoscale constitutive relations and thermal conduction properties of materials are enriched by atomistic information of the underneath lattice microstructure in both bulk elements and interphase cohesive zone. This is accomplished by employing the Cauchy–Born rule, harmonic approximation, and colloidal crystal approximation. A main advantage of the proposed approach is its ability to capture the thermal conduction inside the material interface. The multiscale finite element procedure is performed to simulate an engineering nickel plate specimen with weak interfaces under uni-axial stretch. The simulation results indicate that the crack propagation is slowed down by thermal expansion, and a cooling region is found in the front of crack tip. These phenomena agree with related experimental results. The effect of different loading rates on fracture is also investigated. [DOI: 10.1115/1.4006583]

Keywords: atomistic simulation, fracture, multiscale finite element method, thermomechanical coupling

1 Introduction

Fracture is a very complex multiphysics and multiscale problem that relates to multiple different spatial and temporal scales, multiple different physical fields, and their interactions. In the process of a crack propagation, the interaction between the fine scale random atomistic vibration and macroscale surface separation is manifested by thermal dissipation and heat conduction, which in turn affect the subsequent fracture process. Hence, to study a realistic fracture process of materials, one must consider the temperature effect in order to precisely capture the multiscale energy interaction, dissipation, and release.

In recent years, much success has been made in simulating fracture of metallic materials by brute-force molecular dynamics (MD), which can simulate crack propagation in a solid material system of billions of atoms. Nevertheless, the scale of that system that can be simulated or studied is still in the range of nanoscale to submicron scale, far away from the goal toward to the macroscale engineering design. This has motivated recent developments of multiscale simulation technology, for example, the quasi-continuum (QC) method [1], the virtual-internal-bond (VIB) method [2–4], and Bridging scale method [5], and among many others. A main technical ingredient in all these multiscale methods is the so-called Cauchy–Born rule, which assumes that local deformation in a crystal is uniform and homogeneous, and under such condition or assumption one can link material properties between continuum scale and atomistic scale. However, at the vicinity of a defect, i.e., crack and dislocation sites where the deformation is nonuniform, such assumption is no longer valid.

Recently, Li and his co-workers [6–8] have proposed a multiscale cohesive zone model, which combines the strength of Cauchy–Born rule based atomistic finite element method and the cohesive zone model, and they have successfully simulated fracture processes in polycrystalline solids and other engineering materials.

On the other hand, by taking into account of temperature effect, Liu and Li [9,10] and Yang et al. [11] have also extended the Cauchy–Born rule to finite temperature situations. By adding thermal contribution, they coined the Cauchy–Born rule under such condition as thermal–mechanical Cauchy–Born rule (TCBR). In this paper, a thermomechanical multiscale interphase zone model is proposed to study fracture process under thermomechanical coupling conditions. The proposed method combines the TCBR and the multiscale cohesive zone model, so one can calculate material thermal–mechanical properties in both bulk element and interphase zone. The proposed finite temperature multiscale finite element method has been implemented and validated by applying it to solve a crack propagation problem in a single crystal nickel plate.

The paper is organized into seven sections: we start off Sec. 2 by discussing the thermomechanical Cauchy–Born rule; then, in Sec. 3, we present a mesoscale thermal–mechanical theory inside the interphase zone. The multiscale thermal–mechanical finite element formulation is discussed in Sec. 4, and in Sec. 5, we present a numerical simulation of crack propagation in a single crystal nickel plate. Finally, we conclude the study in Sec. 7.

2 Thermal–Mechanical Cauchy–Born Rule (TMCBR)

Following Refs. [9–11], we first briefly outline the basic assumptions and theory of TCBR in this section. To begin with, we consider the Helmholz free energy of a canonical ensemble at an equilibrium state of finite temperature, which can be written as follows [12]:

$$F_H = -k_B\theta \ln Z = -k_B\theta \ln\left[\int_\Gamma \exp(-H(\mathbf{p},\mathbf{q})/(k_B\theta))d\mathbf{p}d\mathbf{q}\right] \quad (1)$$

where F_H is the Helmholz free energy, k_B Boltzmann constant, θ the temperature of system, Z the partition function, H the

[1]Corresponding author.

Contributed by the Materials Division of ASME for publication in the JOURNAL OF ENGINEERING MATERIALS AND TECHNOLOGY. Manuscript received September 30, 2011; final manuscript received February 28, 2012; published online June 11, 2012. Assoc. Editor: Xin-Lin Gao.

hamiltonian of the system, **p** the position vector of particles, and **q** the momentum vector of particles.

The basic assumptions of TCBR are: (1) the atoms of the system only oscillate near their equilibrium positions, and the motion of atoms is approximated as purely harmonic vibration and (2) the local deformation in the bulk material is assumed to be uniform. Under these conditions, one can obtain the following harmonic approximation of free energy [13–15]

$$F_H(\mathbf{F},\theta) = W_c(\mathbf{F}) + k_B\theta \sum_{i=1}^{N}\sum_{\beta=1}^{n} \ln\left[2\sinh\left(\frac{h\omega_{i\beta}(\mathbf{F})}{4\pi k_B\theta}\right)\right] \tag{2}$$

where $W_c(\mathbf{F})$ is the potential energy at equilibrium state, $\mathbf{F} = \frac{\partial \mathbf{x}}{\partial \mathbf{X}}$ is the deformation gradient, $\omega_{i\beta}$ is the ith frequency of the system in the direction β, which is the eigenvalue of dynamic matrix D, defined as

$$D_{i\alpha j\beta} = \frac{1}{\sqrt{m_i m_j}}\left(\frac{\partial^2 W_c}{\partial x_{i\alpha}\partial x_{j\beta}}\right) \tag{3}$$

Considering

$$F_H = E_{\text{int}} - \theta S \tag{4}$$

where E_{int}, S are the internal energy and entropy of the system, respectively, and substituting Eq. (2) into Eq. (4), the entropy S of the system can be expressed as

$$S = k_B\theta \sum_{i=1}^{N}\sum_{\beta=1}^{n} 2\cot\left(\frac{h\omega_{i\beta}(\mathbf{F})}{4\pi k_B\theta}\right)\frac{h\omega_{i\beta}(\mathbf{F})}{4\pi k_B} - k_B \sum_{i=1}^{N}\sum_{\beta=1}^{n} \ln\left[2\sinh\left(\frac{h\omega_{i\beta}(\mathbf{F})}{4\pi k_B\theta}\right)\right] \tag{5}$$

where N is the total numbers of atoms and n is the number of degrees of freedom for each atom. Based on Eqs. (4) and (5), the internal energy can be also derived as

$$E_{\text{int}} = W_c(\mathbf{F}) + k_B\theta \sum_{i=1}^{N}\sum_{\beta=1}^{n} 2\cot\left(\frac{h\omega_{i\beta}(\mathbf{F})}{4\pi k_B\theta}\right)\frac{h\omega_{i\beta}(\mathbf{F})}{4\pi k_B} \tag{6}$$

So is the specific heat of constant volume C_v

$$C_v = \frac{\partial E_{\text{int}}}{\partial\theta} = k_B\theta \sum_{i=1}^{N}\sum_{\beta=1}^{n}\left(\frac{1}{\sinh^2\left(\frac{h\omega_{i\beta}(\mathbf{F})}{4\pi k_B\theta}\right)}\right)\left(\frac{h\omega_{i\beta}(\mathbf{F})}{4\pi k_B\theta}\right)^2 \tag{7}$$

and the specific heat at constant temperature $\mathbf{C}_T$ as well

$$\mathbf{C}_T = \theta\frac{\partial S}{\partial \mathbf{F}} = -\theta\frac{\partial^2 F_H}{\partial\theta\partial\mathbf{F}} \tag{8}$$

where $\omega_{i\beta}$ are the vibration frequencies of the system, and they are the eigenvalues of the dynamical matrix D defined in Eq. (3). The quasi-harmonic approximation assumes that atoms in the system only oscillate around their equilibrium positions, and we only consider the harmonic part of those oscillations. After finding all the eigenvalues of dynamic matrix, we make further simplifications upon the harmonic approximation by neglecting all coupling modes of vibrations among different atoms, and we assume that all the atoms have the same vibration mode in different coordinate direction. Based on these simplifications, we may assume that the harmonic approximation may be localized in each unit cell, and by doing so we make it consistent with the Cauchy–Born rule. This *localized harmonic approximation* is a very strong assumption, and it may or may not be hold in practical problems.

However, if we adopt the assumption, and then it makes sense to discuss the Helmholtz free energy in a unit cell, which can be cast into the following form:

$$F_H^{uc} = W_{uc}(\mathbf{F}) + nk_B\theta \sum_{i=1}^{n_{\text{bound}}} \ln\sinh\left[\frac{hD_i^{\frac{1}{2n}}}{2\pi k_B\theta}\right] \tag{9}$$

where potential energy W_{uc} is

$$W_{uc}(\mathbf{F}) = \sum_{l=1}^{n\text{bond}} \phi(r_l) \tag{10}$$

Note that the unit cell of a Bravais lattice is a primitive cell, which only considers the nearest neighbor interaction. However, the unit cell referred in Eq. (9) should not be understood as a primitive cell in a Bravais lattice. This is because that the small number of atoms in a primitive cell may not be capable of consisting of an equilibrium ensemble or even a local equilibrium region. In general, we need include long range multibody interactions even for a local canonical ensemble. In this work, however, we postulate an *idealization* that is coined as *consistently localized harmonic approximation in Cauchy continuum* (CLHACC). In such ideal case, one may take a primitive cell in a Bravis lattice as an *effective local canonical ensemble*. This is an additional strong assumption on the local equilibrium approximation (LEA), e.g., Ref. [16], which implies that not only the mean displacement field (coarse scale) is uniform, the fluctuation displacement field (the fine scale) is also locally self-similar in a local region.

Under such assumption and in the classical limit, we have

$$\sinh\left(\frac{h\omega_{i\beta}}{4\pi k_B\theta}\right) \approx \frac{h\omega_{i\beta}}{4\pi k_B\theta} \tag{11}$$

and

$$C_v = nk_B n_{\text{bound}} \tag{12}$$

subsequently, the Helmholz free energy in a unit cell, i.e., Eq. (9), becomes

$$F_H^{uc} = W_{uc}(\mathbf{F}) + nk_B\theta \sum_{i=1}^{n_{\text{bound}}} \ln\left[\frac{hD_i^{\frac{1}{2n}}}{2\pi k_B\theta}\right] \tag{13}$$

where

$$D_i = \left(\prod_{\beta=1}^{n}\omega_{i\beta}\right)^2 \tag{14}$$

The first Piola–Kirchihoff stress (PK-I) can be written as

$$\mathbf{P} = \frac{1}{\Omega_0^{\text{unit}}}\frac{\partial {F_H}^{uc}}{\partial\mathbf{F}} = \frac{1}{\Omega_0^{\text{unit}}}\frac{\partial W_{uc}(\mathbf{F})}{\partial\mathbf{F}} + \frac{k_B\theta}{2\Omega_0^{\text{unit}}}\sum_{i=1}^{n_{\text{bound}}}\frac{1}{D_i}\frac{\partial D_i}{\partial\mathbf{F}} \tag{15}$$

The second term in the above equation is the thermal stress that is caused by increase of temperature. From this equation, we can calculate macro stress for any crystalline materials based on average elastic energy density in a single Bravais unit cell.

For example in Fig. 1 [17], we consider a two-dimensional hexagonal lattice unit cell. Based on the microstructure of the unit cell, PK-I stress tensor, Eq. (15), becomes

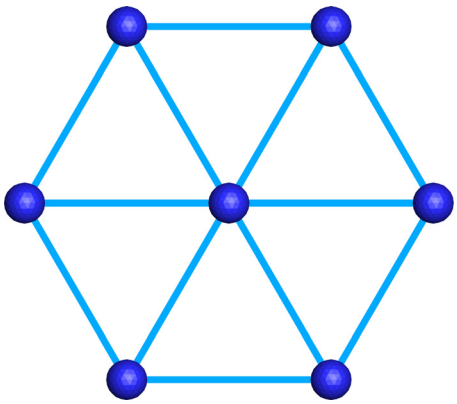

Fig. 1 The unit cell for 2D hexagonal lattice

$$\mathbf{P} = \frac{1}{\Omega_0^{\text{unit}}} \sum_{l=1}^{n_{\text{bond}}} \frac{\partial \phi}{\partial r_l} \frac{\mathbf{r}_l \otimes \mathbf{R}_l}{r_l} + \frac{k_B T}{2\Omega_0^{\text{unit}}} \sum_{i=1}^{N} \frac{1}{D_i} \frac{\partial D_i}{\partial \mathbf{F}} \tag{16}$$

Only the center atom is considered in 2D hexagonal unit cell for calculating the dynamic matrix, so the dynamic matrix becomes

$$D_{\alpha\beta} = \frac{1}{m_c} \left(\frac{\partial^2 W_{uc}}{\partial x_{l\alpha} \partial x_{l\beta}} \right) = \frac{1}{m_c} \sum_{l=1}^{n\text{bond}} \left(\frac{\partial^2 \phi(r_l)}{\partial r_l^2} \frac{x_{l\alpha} x_{l\beta}}{r_l^2} - \frac{\partial \phi(r_l)}{\partial r_l} \frac{x_{l\alpha} x_{l\beta}}{r_l^3} + \frac{\partial \phi(r_l)}{\partial r_l} \frac{\delta_{\alpha\beta}}{r_l} \right) \tag{17}$$

3 Thermal–Mechanical Couplings in Interphase Elements

The multiscale finite element model proposed in this work contains two types of elements: (1) the bulk element, and (2) the interphase element. The interphase element is a narrow strip that forms a subscale buffer zone between any pair of bulk elements.

To distinguish our approach with the conventional cohesive zone model, in which the cohesive zone is a virtual entity that has no width, we label the finite width interface element in the proposed multiscale finite element method as the *interphase element* or *interphase zone*.

We assume that the deformation inside the bulk element is uniform, so that we can apply the thermal–mechanical Cauchy–Born rule to calculate its stress state if we know the deformation gradient of each element. On the other hand, the deformation inside the interphase element is highly nonlinear and nonuniform, so one cannot apply the Cauchy–Born rule to calculate stresses (see Fig. 2). Moreover, one may not be able to use harmonic approximation inside the interphase element, because of the drastic deformation and atomistic bond breaking inside the interphase element. In this section, we discuss how to calculate stress, deformation, temperature, and thermal–mechanical couplings inside interphase elements.

3.1 Stress Calculation in the Interphase Zone. In principle, a Cauchy–Born based coarse grained continuum formulation is not adequate for an accurate calculation of stress distribution inside the interphase element, because of its nonlinear, nonuniform, and an-harmonic characters.

One way to improve the accuracy but still using finite element continuum approach is to adopt high order interpolation field instead of linear interpolation. The justification is as follows: For linear interpolation field in an element, one can use only one quadrature point for complete integration. In the multiscale finite element method (FEM) formulation, this is equivalent to carry out a molecular dynamics (MD) computation for one unit cell per element. If we continuously increase the order of interpolation and hence the number of quadrature points, we will need to carry out MD calculations in more and more unit cells per element, and consequently the calculation may become more and more accurate. This approach could easily capture the nonuniform deformation of one element.

To capture the nonlinear and an-harmonic responses inside the interphase zone, we adopt a so-called colloidal crystal approach. The colloidal crystal approach in this work is different from what is discussed in Refs. [18,19]. In the proposed crystal approach, we retain the original lattice structure but we use the colloidal depletion potential to replace the original atomistic bond potential, and the coarse grain depletion potential in interphase zone can be obtained by the following analytical integration [20]

$$\phi_{\text{depl}}(r) = \int_{\text{halfspace}} \beta \phi_{\text{bulk}}(r - r') dV' \tag{18}$$

where ϕ_{bulk} is the potential of bulk materials and β is the number of atoms per volume.

It should be noted that the deformation gradient inside the interphase zone is not constant, because the deformation is nonuniform. In this paper, we use the bilinear FEM shape function of quadrilateral elements in interphase zone. Therefore, the deformation gradient inside the interphase zone is a linear function of the position vector $\mathbf{X}$, i.e., $\mathbf{F}_{\text{intp}} = \mathbf{F}_{\text{intp}}(\mathbf{X})$. We can then calculate the stress at each quadrature point inside the interphase element by averaging atomistic bond force in a unit cell as shown in Eq. (15). However, this may cause shear locking in the interphase zone and ill-condition of the stiffness matrix. This is because the aspect ratio of the interphase element is too large, $L/R \rightarrow 10^3$–10^5.

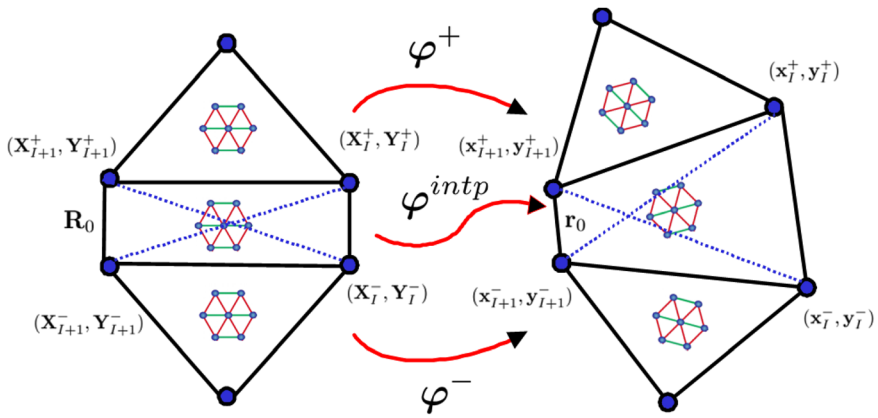

Fig. 2 Deformation of the interphase zone

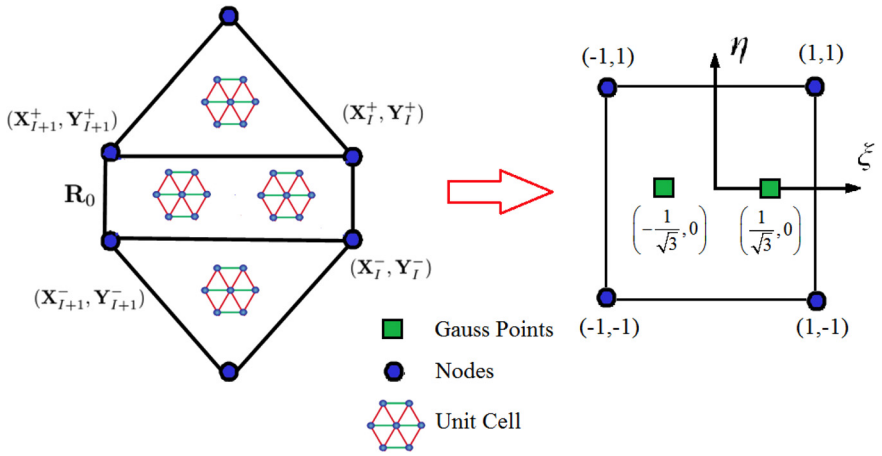

Fig. 3 Linear quadrilateral element for the interphase zone

To avoid shear locking inside the interphase zone, in this work we adopt the reduced integration technique to integrate the weak form inside the interphase zone. Instead of using standard four quadrature points, we only use two quadrature points in each interphase element as shown in Fig. 3. Each quadrature point is corresponding to a unit cell. By doing so, we can capture some nonuniform deformations in the interphase element and also avoid the unstable (hour-glass mode) results that is caused by zero energy mode of a first order approximation (one quadrature point integration) [21].

3.2 Governing Equations of Thermomechanical Interphase Zone Model. In nonlinear continuum mechanics, the equation of motion can be written as

$$\nabla \cdot \mathbf{P} + \rho_0 \mathbf{b} - \rho_0 \ddot{\mathbf{u}} = 0 \tag{19}$$

where $\mathbf{P}$ is the first Piola–Kirchhoff stress, $\mathbf{b}$ is the body force, ρ_0 is the density at initial configuration, and $\mathbf{u}$ is the displacement.

According to the first law of thermodynamics, the rate of internal energy in a continuum system is

$$\frac{D\varepsilon}{Dt} = \mathbf{P} : \dot{\mathbf{F}} - \nabla \cdot \mathbf{q} + \rho_0 Q \quad \text{(bulk zone)} \tag{20}$$

and the rate of internal energy in the interphase zone is

$$\frac{D\varepsilon}{Dt} = \mathbf{P} : \dot{\mathbf{F}} - \nabla \cdot \mathbf{q} \quad \text{(interphase zone)} \tag{21}$$

where Q is the internal heat source and $\mathbf{q}$ is heat flux.

We neglect the heat generation in the interphase zone due to the interphase zone is very thin, and substitute Eq. (6) into Eqs. (20) and (21), we have

$$\frac{1}{\Omega_0^{\text{unit}}}\left(\mathbf{C}_T : \dot{\mathbf{F}} + C_v \dot{\theta}\right) = -\nabla \cdot \mathbf{q} + \rho Q = k\nabla^2\theta + \rho Q(t) \quad \text{(bulk zone)} \tag{22}$$

and

$$\frac{1}{\Omega_0^{\text{unit}}}\left(\mathbf{C}_T : \dot{\mathbf{F}} + C_v \dot{\theta}\right) = -\nabla \cdot \mathbf{q} = k\nabla^2\theta \quad \text{(interphase zone)} \tag{23}$$

3.3 Heat Generation in the Interphase Zone. The mechanical energy release due to the breaking of interphase zone is

$$\Gamma = \int_0^{\Delta_{\max}} \mathbf{T} \cdot d\boldsymbol{\Delta} \tag{24}$$

where T is the traction force along the boundary of interphase zone and bulk element, and $\boldsymbol{\Delta}$ is the separation of the interphase zone, and $\Delta_{\max}$ is the maximum separation of the interphase zone. Hence, the energy release rate in the interphase zone will be

$$\dot{\Gamma} = \mathbf{T} \cdot \dot{\boldsymbol{\Delta}} \rightarrow d\dot{\Gamma} = \mathbf{T} \cdot d\dot{\boldsymbol{\Delta}}. \tag{25}$$

In this work, we assume that all the mechanical fracture energy completely convert to heat without any loss or save to other form of potential energies in the process of fracture. The fracture of the interphase zone will then cause temperature rise inside the interphase zone as well as strong thermal induced deformation, which is equivalently manifested as both displacement jump as well as a temperature jump at the two sides of the interphase zone. Therefore, we postulate that

$$\int_{\partial\Omega^{i+}_{\text{intp}}} \mathbf{T} \cdot d\dot{\boldsymbol{\Delta}} dS = \int_{\Omega^i_{\text{intp}}} \frac{1}{\Omega_0^{\text{unit}}} (\mathbf{C}_T : \dot{\mathbf{F}} + C_v \dot{\theta}) d\Omega \tag{26}$$

where $\partial\Omega^{i+}_{\text{intp}}$ is just one side of boundary of the interphase element i, i.e., $\partial\Omega^i_{\text{intp}} = \partial\Omega^{i+}_{\text{intp}} \bigcup \partial\Omega^{i-}_{\text{intp}}$.

3.4 Heat Conduction in Interphase Zone. Because it is difficult to determine k_{intp} inside the interphase zone, we adopt an approximation that convert the weak form of heat conduction term inside the interphase zone into the following boundary integral:

$$\int_{\Omega^i_{\text{intp}}} k_{\text{intp}} \nabla\theta \nabla\delta\theta d\Omega = \int_{\partial\Omega^{i+}_{\text{intp}}} \mathbf{q}_{\text{intp}} \cdot \mathbf{n} \delta\theta dS \tag{27}$$

Again here, $\partial\Omega^{i+}_{\text{intp}}$ is just half of the interphase element boundary, and the total boundary is $\partial\Omega^i_{\text{intp}} = \partial\Omega^{i+}_{\text{intp}} \bigcup \partial\Omega^{i-}_{\text{intp}}$.

Depending on the interphase zone's damage state, i.e., partially open or completely open, the heat flux across the interphase zone can be written as

$$\mathbf{q}_{\text{intp}} = h_{\text{intp}} \Delta\theta \mathbf{n} \tag{28}$$

where $\Delta\theta$ is the temperature jump, and h_{intp} is the heat conduction of interphase zone.

In this work, we adopt an approach that is similar to that used in Ref. [22], and the interphase heat conductance is chosen as follows:

$$h_{\text{inpt}} = sh_{i,\text{inpt}} + (1-s)\frac{[k_{g,0} + C_g\theta]}{\eta}, \quad s > s_c \tag{29}$$

where $h_{i,\text{inpt}}$ is the initial interphase conductance and $h_{i,\text{air}} = [k_{g,0} + C_g\theta]/\eta$, which is the ratio of gas conductivity and the effective crack (normal) opening length η. The parameter s is an indicator to measure the damage state of the interphase, which is calculated by the average stretched bond length inside the interphase zone, i.e.,

$$s = \frac{R_0}{\bar{r}}$$

where $\bar{r}$ is the average stretched bond length inside the interphase zone. When $\bar{r} \gg R_0$, $s \to 0$, i.e., the interphase is completely opened or being fractured. In actual computation, when $s \to 0$ or $s < s_c$, we take the thermal conductance of the interphase zone $h_{\text{inpt}} = 0$, because we assume that the gas conductance is far smaller than crystalline thermal conductance, its effect can be neglected.

4 Finite Element Galerkin Weak Formulation for Multiscale Interphase Zone Model

In the following, we present the Galerkin variational weak formulation of the proposed finite temperature multiscale interphase zone method. Denote the domain of interests in the reference configuration as Ω_0. In two-dimensional space, we can discrete it in a set of disjoined triangle bulk elements, Ω^e, $e = 1, 2, \ldots n^b_{\text{elem}}$, and a set of disjoined quadrilateral interphase element Ω^i, $i = 1, 2, \ldots, n^c_{\text{elem}}$, such that

$$\Omega_0 = \left(\bigcup_{e=1}^{n^b_{\text{elem}}} \Omega^e_b\right) \bigcup \left(\bigcup_{i=1}^{n^c_{\text{elem}}} \Omega^i_c\right) \tag{30}$$

Note that mathematically or topologically the set of triangle elements and quadrilateral elements may not be able to form a compact cover of Ω_0, because there could be a tiny hole in the vertex of the triangle elements, if all the elements are within the same scale. Nevertheless, Eq. (30) is essentially a physical statement rather than a mathematical statement. We may interpret the mesh as a multiscale mesh, which means that at macroscale the set of triangle elements forms a mathematical cover of Ω_0, but zooming in the fine scale one may find an interphase quadrilateral layer between two adjacent macroscale triangle elements.

With the aid of trail function $\mathbf{u}^h$ and test function $\delta\mathbf{u}^h$, a Lagrangian type of Galerkin Lagrangian weak formulation may be expressed as follows:

$$\begin{aligned}
&\sum_{e=1}^{n^b_{\text{elem}}} \left\{ \int_{\Omega^e_b} \rho_0 \ddot{\mathbf{u}}^h \cdot \delta\mathbf{u}^h d\Omega + \int_{\Omega^e_b} \mathbf{P} : \delta\mathbf{F}^h d\Omega \right\} \\
&\quad + \sum_{i=1}^{n^c_{\text{elem}}} \left\{ \int_{\Omega^i_c} \rho_0 \ddot{\mathbf{u}}^h \cdot \delta\mathbf{u}^h d\Omega + \int_{\Omega^i_c} \mathbf{P} : \delta\mathbf{F}^h d\Omega \right\} \\
&\quad = \sum_{e=1}^{n^b_{\text{elem}}} \left\{ \int_{\Omega^e_0} \mathbf{b} \cdot \delta\mathbf{u}^h d\Omega + \int_{\partial_t\Omega^e_0} \overline{\mathbf{T}} \cdot \delta\mathbf{u}^h dS \right\} + \sum_{i=1}^{n^c_{\text{elem}}} \int_{\Omega^i_c} \mathbf{b} \cdot \delta\mathbf{u}^h dV
\end{aligned} \tag{31}$$

where $\mathbf{b}$ is the body force, Ω^e_b is the eth bulk element, $\partial_t\Omega^e_b$ is the interception between the traction boundary and the boundary of the eth element, and Ω^i_c is the ith interphase element. The interphase element does not overlap with traction boundary.

Assume that there is no heat source or sink in the computational domain. The weak form of energy equation can be written as

$$\begin{aligned}
&\sum_{e=1}^{n^b_{\text{elem}}} \left\{ \int_{\Omega^e_b} k\nabla\theta \cdot \nabla\delta\theta d\Omega \right\} + \sum_{i=1}^{n^c_{\text{elem}}} \left\{ \int_{\Omega^i_c} k_{\text{intp}} \nabla\theta \cdot \nabla\delta\theta d\Omega \right\} \\
&\quad + \sum_{e=1}^{n^b_{\text{elem}}} \int_{\Omega^e_b} \frac{1}{\Omega^{\text{unit}}_0} \left(\mathbf{C}_T : \dot{\mathbf{F}} + C_v\dot{\theta} \right) \delta\theta d\Omega \\
&\quad + \sum_{i=1}^{n^c_{\text{elem}}} \int_{\Omega^i_c} \frac{1}{\Omega^{\text{unit}}_0} \left(\mathbf{C}^{\text{intp}}_T : \dot{\mathbf{F}} + C^{\text{intp}}_v\dot{\theta} \right) \delta\theta d\Omega \\
&\quad = \sum_{e=1}^{n^b_{\text{elem}}} \int_{\partial_t\Omega^e_b} \overline{\mathbf{q}} \cdot \mathbf{n} \delta\theta dS
\end{aligned} \tag{32}$$

where $\partial_t\Omega^e_b$ is the intersection between $\partial\Omega^e_b$ and $\partial\Omega^q_0$, which is the heat flux boundary.

In Section 3, we have derived that

$$\begin{aligned}
\int_{\partial\Omega^{i+}_c} \mathbf{T} \cdot d\dot{\boldsymbol{\Lambda}} \delta\theta dS &= -\int_{\partial\Omega^{e+}_b} \mathbf{T} \cdot d\dot{\boldsymbol{\Lambda}} \delta\theta dS \\
&= \int_{\Omega^i_c} \frac{1}{\Omega^{\text{unit}}_0} (\mathbf{C}_T : \dot{\mathbf{F}} + C_v\dot{\theta}) \delta\theta d\Omega
\end{aligned} \tag{33}$$

and

$$\int_{\partial\Omega^{i+}_c} \mathbf{q}_{\text{intp}} \cdot \mathbf{n} \delta\theta dS = -\int_{\partial\Omega^{e+}_b} \mathbf{q}_{\text{intp}} \cdot \mathbf{n} \delta\theta dS = \int_{\Omega^i_c} k_{\text{intp}} \nabla\theta \nabla\delta\theta d\Omega \tag{34}$$

The weak form for energy equation becomes

$$\begin{aligned}
&\sum_{e=1}^{n^b_{\text{elem}}} \left\{ \int_{\Omega^e_b} k\nabla\theta \cdot \nabla\delta\theta d\Omega \int_{\Omega^e_b} \frac{1}{\Omega^{\text{unit}}_0} \left(\mathbf{C}_T : \dot{\mathbf{F}} + C_v\dot{\theta} \right) \delta\theta d\Omega \right\} \\
&= \sum_{e=1}^{n^b_{\text{elem}}} \left\{ \int_{\partial_t\Omega^e_b} \overline{\mathbf{q}} \cdot \mathbf{n} \delta\theta dS + \int_{\partial\Omega^{e+}_b} \mathbf{q}_{\text{intp}} \cdot \mathbf{n} \delta\theta dS + \int_{\partial\Omega^{e+}_b} \mathbf{T} \cdot d\dot{\boldsymbol{\Lambda}} \delta\theta dS \right\}
\end{aligned} \tag{35}$$

where $\mathbf{q}_{\text{intp}} \cdot \mathbf{n} = h_{\text{intp}}(\theta)\Delta\theta$, and $\Delta\theta$ is the temperature jump across the interphase zone.

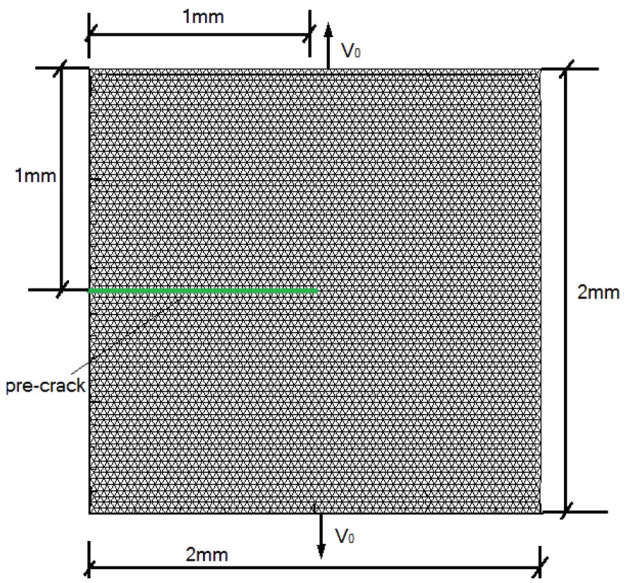

Fig. 4 Finite element mesh

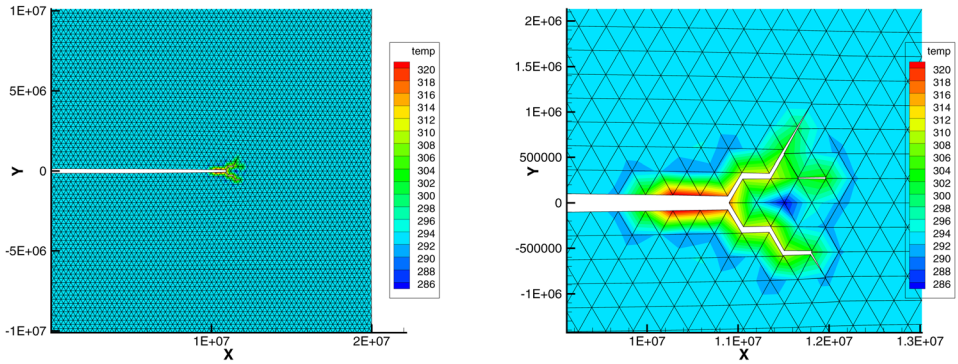

(a) Whole specimen (b) Crack tip

Fig. 5 Temperature distribution at time 0.14 μs (V_0: 100 m/s, T_0: 293 K)

4.1 Continuum Multiscale Finite Element Formulation. Consider the finite element interpolation representation

$$\mathbf{u}^h = \sum_e \mathbf{N}(\xi,\eta,\zeta)\mathbf{d}_e(t) = \sum_e \sum_{I=1}^{N_e} N_I \mathbf{d}_I \tag{36}$$

where $\mathbf{N}$ is the shape function and $\mathbf{d}_I$ is nodal displacement. Following the standard FE discretization procedure, e.g., Ref. [23], we have the following discrete equations of motion

$$\mathbf{M}\ddot{\mathbf{d}} + \mathbf{f}^{\text{int}}(\mathbf{d}) = \mathbf{f}^{\text{ext}} \tag{37}$$

where

$$\mathbf{M} = \mathop{\mathbf{A}}_{e=1}^{n^b_{\text{elem}}} \int_{\Omega^e_0} \rho_0 \mathbf{N}^{eT}\mathbf{N}^e dV + \mathop{\mathbf{A}}_{i=1}^{n^c_{\text{elem}}} \int_{\Omega^i_0} \rho_0 \mathbf{N}^{iT}\mathbf{N}^i dV \tag{38}$$

$$\mathbf{f}^{\text{int}} = \mathop{\mathbf{A}}_{e=1}^{n^b_{\text{elem}}} \int_{\Omega^e_0} \mathbf{B}^{eT}\mathbf{P}^e(\mathbf{d}) dV + \mathop{\mathbf{A}}_{i=1}^{n^c_{\text{elem}}} \int_{\Omega^i_0} \mathbf{B}^{iT}\mathbf{P}^i(\mathbf{d}) dV \tag{39}$$

$$\mathbf{f}^{\text{ext}} = \mathop{\mathbf{A}}_{e=1}^{n^b_{\text{elem}}} \left\{ \int_{\Omega^e_b} \mathbf{N}^{eT}\mathbf{B}^e dV + \int_{\partial_t B^e_b} \mathbf{N}^{eT}\bar{\mathbf{T}}^e dS \right\} + \mathop{\mathbf{A}}_{i=1}^{n^c_{\text{elem}}} \int_{\Omega^i_0} \mathbf{N}^{iT}\mathbf{B}^i dV \tag{40}$$

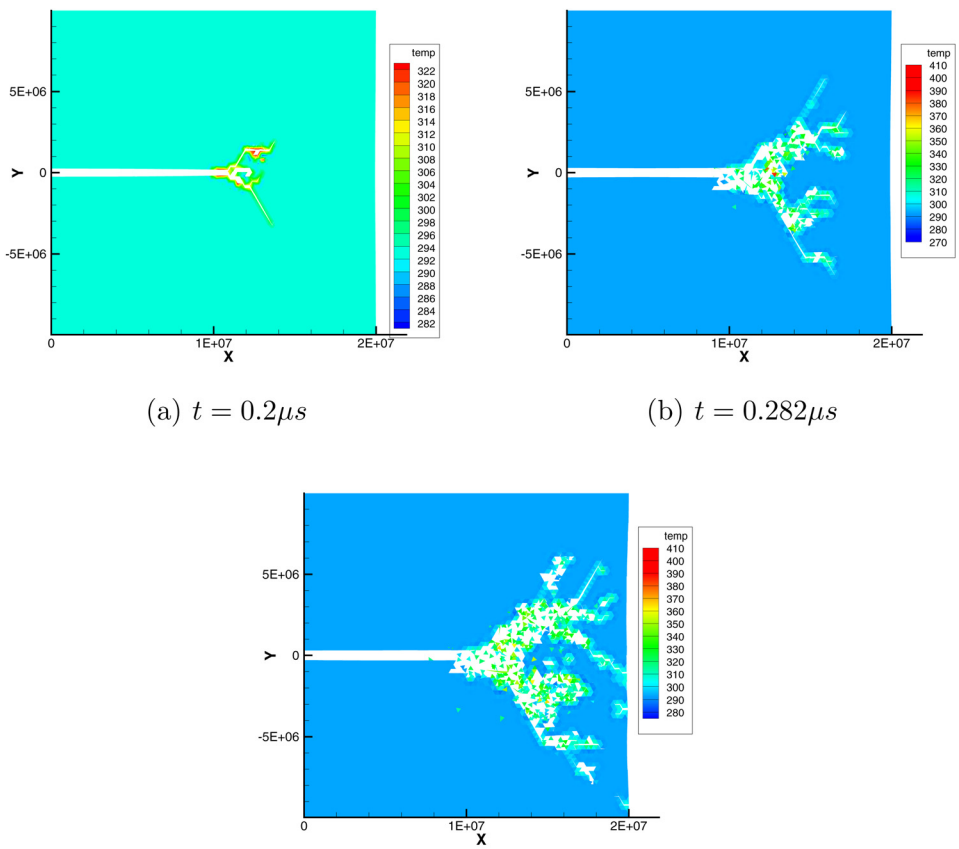

(a) $t = 0.2\mu s$ (b) $t = 0.282\mu s$

(c) $0.332\mu s$

Fig. 6 Temperature distribution at different time (V_0: 100 m/s, T_0: 293 K)

where $\boldsymbol{A}$ is the element assemble operator, $\mathbf{N}^e$ is the element shape function matrix, and $\mathbf{B}^e$ is the element B-matrix.

4.2 Finite Element Formulation for Heat Transfer. Let

$$\theta(x,t) = \sum_e \mathbf{N_T}(\xi,\eta,\zeta)\theta_e(t) = \sum_e \sum_{I=1}^{N_e} N_{TI}\theta_I \tag{41}$$

where $\mathbf{N_T}$ is the shape function, and θ_I is nodal temperature. Then, we have the discrete dynamic equations for heat conduction

$$[\mathbf{C_v}][\dot{\boldsymbol{\theta}}] + [\mathbf{C_T}][\dot{\mathbf{d}}] + [\mathbf{K}][\boldsymbol{\theta}] = \mathbf{Q}_{\text{body}} + \mathbf{Q}_{\text{bound}} + \mathbf{Q}_{\text{inpt}} + \mathbf{Q}_{\text{frac}} \tag{42}$$

where θ is the global temperature vector, and

$$\mathbf{C}_v = \underset{e=1}{\overset{n^b_{\text{elem}}}{\boldsymbol{A}}} \left[\int_{\Omega^e_b} \frac{1}{\Omega^e_b} C_v \mathbf{N}_T^T \mathbf{N}_T d\Omega \right] \tag{43}$$

$$\mathbf{C}_T = \underset{e=1}{\overset{n^b_{\text{elem}}}{\boldsymbol{A}}} \left[\int_{\Omega^e_b} \frac{1}{\Omega^e_b} [\mathbf{C}_{eT}] \mathbf{N}_T^T \frac{\partial \mathbf{N}}{\partial \mathbf{R}} d\Omega \right] \tag{44}$$

$$\mathbf{K} = \underset{e=1}{\overset{n^b_{\text{elem}}}{\boldsymbol{A}}} \left[\int_{\Omega^e_b} k \frac{\partial \mathbf{N}_T^T}{\partial \mathbf{R}} \frac{\partial \mathbf{N}_T}{\partial \mathbf{R}} d\Omega \right] \tag{45}$$

$$\mathbf{Q}_{\text{bound}} = \underset{e=1}{\overset{n^b_{\text{elem}}}{\boldsymbol{A}}} \left[\int_{\partial\Omega^e_q} \mathbf{N}_T^T \overline{\mathbf{q}} \cdot \mathbf{n} dS \right] \tag{46}$$

$$\mathbf{Q}_{\text{intp}} = \underset{e=1}{\overset{n^b_{\text{elem}}}{\boldsymbol{A}}} \left[\int_{\partial\Omega^e_b} \mathbf{N}_T^T h_{\text{inpt}} \Delta\theta dS \right] \tag{47}$$

$$\mathbf{Q}_{\text{frac}} = \underset{e=1}{\overset{n^b_{\text{elem}}}{\boldsymbol{A}}} \int_{\partial\Omega^e_b} \mathbf{N}_T^T \mathbf{T}(\delta(t)) \cdot \dot{\delta}(t) dS \tag{48}$$

where $\mathbf{C}_v$ is the global specific heat matrix at constant volume, $\mathbf{C}_T$ is the global specific heat matrix at constant temperature, $\mathbf{K}$ is the global thermal conductivity matrix, $\mathbf{Q}_{\text{bound}}$ is the global external heat load vector due to external heat flux, $\mathbf{Q}_{\text{intp}}$ is the global heat load vector which go through interphase zone due to thermal conduction, $\mathbf{Q}_{\text{frac}}$ is the global heat load vector that is caused by fracture energy, and $\mathbf{n}$ is the unit out normal vector of boundary surface.

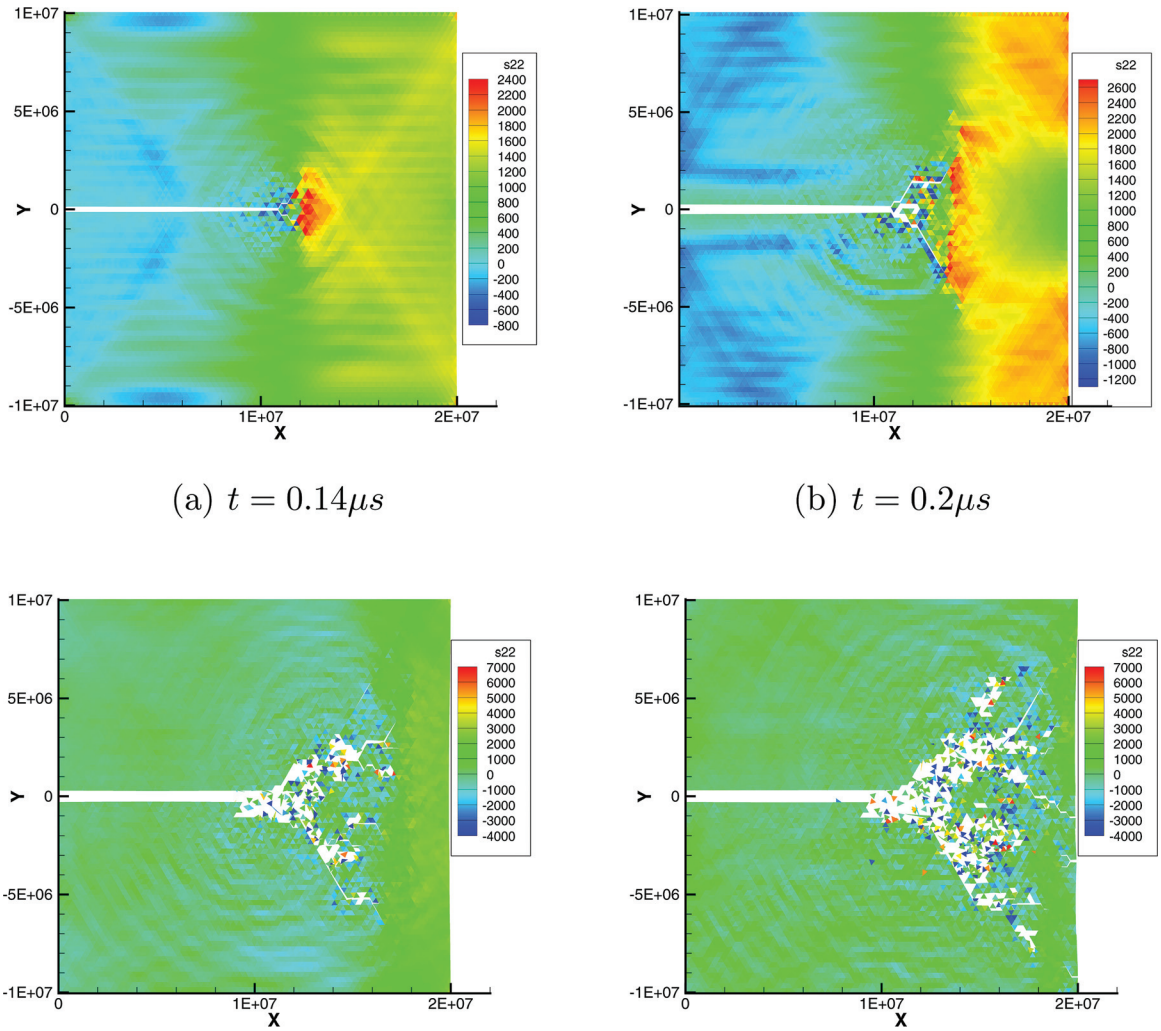

(a) $t = 0.14\mu s$ (b) $t = 0.2\mu s$

(c) $t = 0.282\mu s$ (d) $t = 0.332\mu s$

Fig. 7 Stress (σ_{22}) distribution at different time (0.83027 × 10^7 Pa) (V_0: 100 m/s, T_0: 293 K)

5 Numerical Examples

In this section, we report some preliminary results of a numerical example where simulations of thermal–mechanical fracture of a nickel plate is performed. The facture process of the nickel plate is simulated by using the proposed thermal-mechanical Cauchy-Born (TMCB) interphase zone model. The nickel plate has an in-plane dimension of 2 mm × 2 mm, a precrack is set in the middle of the plate (see Fig. 4). The finite element discretization model of the plate contains 10,032 triangle bulk elements and 15,000 interphase zone elements. All the material properties, such as specific heat, are calculated according to the above theory, except thermal conductivity k and thermal conduction h_{inpt} of the interphase zone. In fact, the value of macro experiments $k = h_{\text{intp}} = 90$ W/(m · K) is adopted due to the difficulty in calculating the thermal conductivity based on thermodynamics.

The plate is subjected to a constant velocity V_0 boundary condition at its top and bottom sides, so it is being stretched in the vertical direction (see Fig. 4); $\delta t = 1.0 \times 10^{-10}$ s is chosen as the time step for time integration. A standard Lennard-Jones (L-J) potential (Eq. (49)) is used to describe the interaction between atoms in the bulk, with $\epsilon = 0.5188$ eV, $\sigma = 2.28$ Å

$$\phi(r) = 4\epsilon\left[\left(\frac{\sigma}{r}\right)^{12} - \left(\frac{\sigma}{r}\right)^{6}\right] \tag{49}$$

For the interphase zone in nickel plate, the depletion potential (Eq. (50)) can be obtained by substituting Eq. (49) into Eq. (18).

$$\phi_{\text{depl}}(r) = \frac{\pi\epsilon}{\sqrt{2}}\left[\frac{1}{45}\left(\frac{\sigma}{r}\right)^{9} - \frac{1}{3}\left(\frac{\sigma}{r}\right)^{3}\right] \tag{50}$$

To investigate the effect of the interphase zone on fracture process, an artificially lowered potential-well of the interphase zone, 0.1620 eV, is used in the simulation. Except the potential-well, the other parameters of interphase zone are the same as the bulk.

Figures 5 and 6 display the temperature distribution on a fractured nickel plate in the case of the loading rate at 100 m/s. A local region of temperature cooling in front of the crack tip can be found while the crack is propagating. In fact, from Fig. 5 (a snapshot at $t = 0.14$ μs), one may find that (i) a temperature increase of 27 K at the crack tip, and (ii) a 7 K temperature drop at a region between the two bifurcated cracks. This result agrees with the experiment results reported in Ref. [24], and it is also very similar to the simulation results reported in Ref. [25]. The explanation to this is that the speed of crack propagation and stress wave is much higher than that of thermal conduction. When the interphase zone fractures, the mechanical energy release converts to heat or crack surface temperature rise on one hand, and on the other hand, it

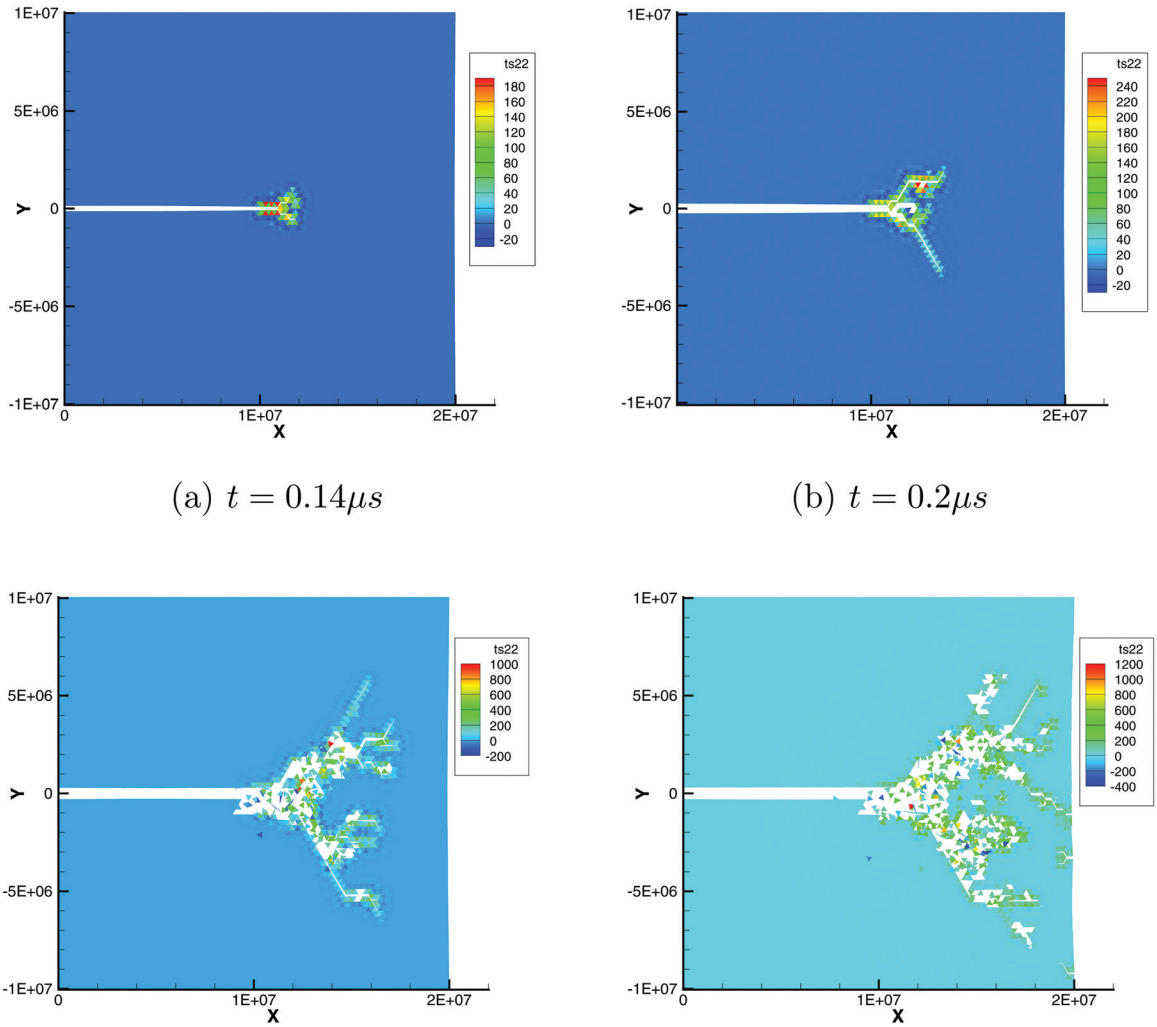

(a) $t = 0.14\mu s$ (b) $t = 0.2\mu s$

(c) $t = 0.282\mu s$ (d) $t = 0.332\mu s$

Fig. 8 Thermal stress (σ_{22}) distribution at different time (0.83027 × 10^7 Pa) (V_0: 100 m/s, T_0: 293 K)

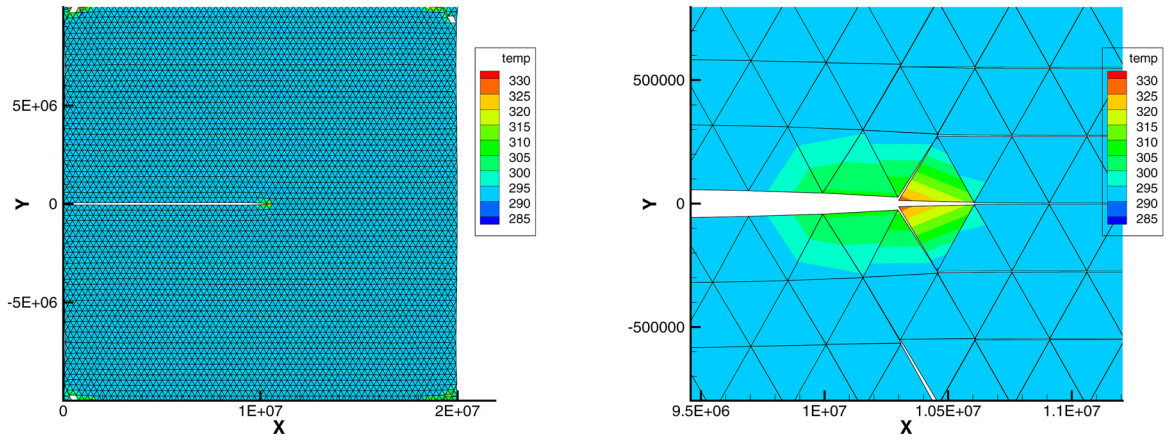

(a) all model (b) Crack tip

Fig. 9 Temperature distribution at time 0.084 μs (V_0: 400 m/s, T_0: 293 K)

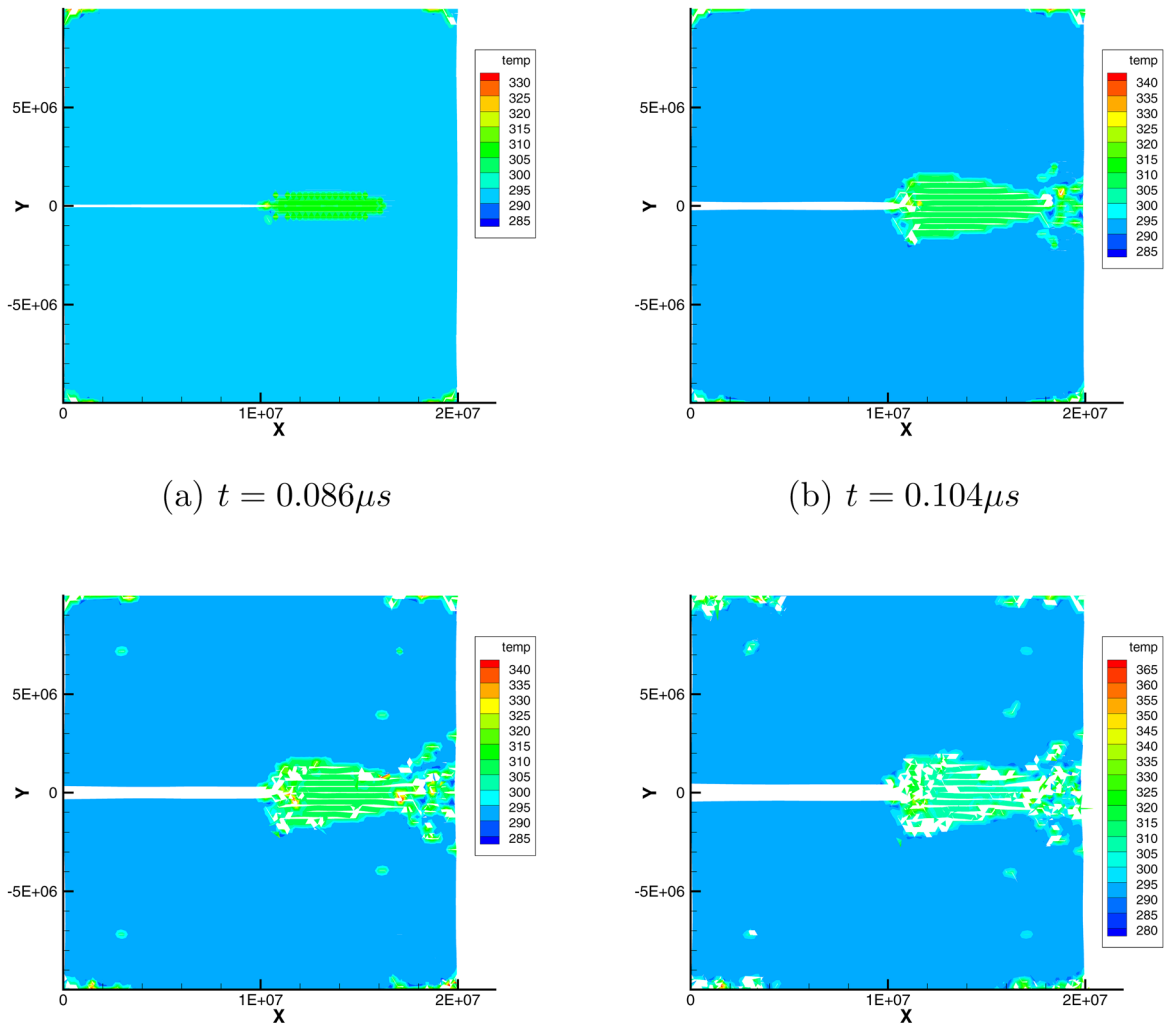

(a) $t = 0.086\mu s$ (b) $t = 0.104\mu s$

(c) $t = 0.118\mu s$ (d) $t = 0.134\mu s$

Fig. 10 Temperature distribution at different time (V_0: 400 m/s, T_0: 293 K)

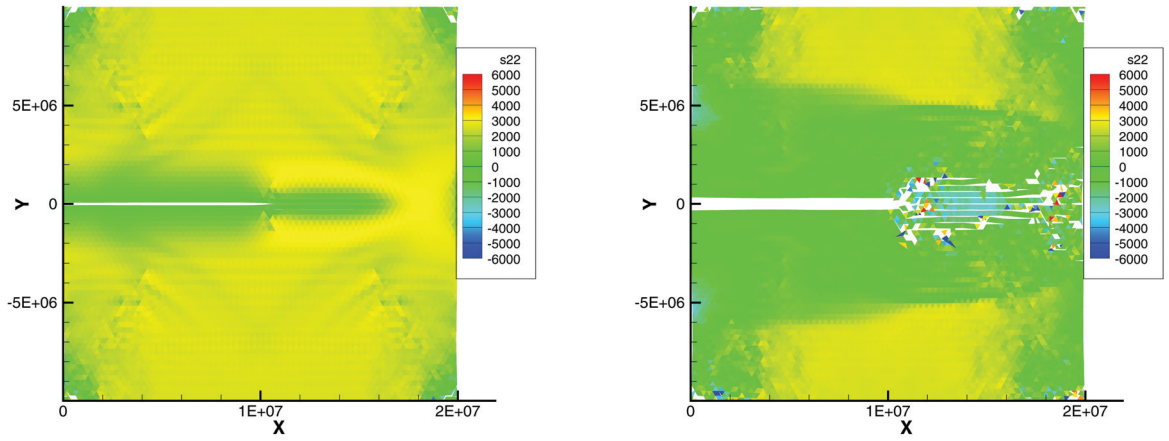

(a) $t = 0.086\mu s$ (b) $t = 0.118\mu s$

Fig. 11 Stress (σ_{22}) distribution at different time (0.83027 × 10^7 Pa) (V_0: 400 m/s, T_0: 293 K)

will also suck mechanical energy toward to the crack tip, which, due to the thermal–mechanical coupling, will also create a heat flux flow toward to the crack tip as well. This will transfers the energy from the further away region to the nearer adjacent region of the crack tip. If we compare the thermal stress distribution (Fig. 8) with the mechanical stress distribution (Fig. 7), we found that the thermal stress (Fig. 8) only exists in the local regions near the crack, but the magnitude of the thermal stress is far lower than that of the mechanical stress. This characteristics of the stress distribution will leas crack bifurcation; and this may explain why there are so many fragments if we continue to apply load. This phenomenon is different from the fragmentation simulation result obtained by penetration that does not take into account temperature effect [6]. Figures 9, 10, and 12 display the temperature distribution in a specimen that is under stretching rate of 400 m/s. Comparing it with the case of the stretching rate of 100 m/s, one may find that the onset fracture time is obviously affected by the loading rate and temperature. The onset time of fracture for high loading rate is much earlier than that of low loading rate. It is also found that the mode of the fracture is different for different loading rates. In the case of the loading rate at 400 m/s (Fig. 11) the stress waves will first collide with each other in the middle of plate before the crack propagates, this collision causes high tensile stress wave at the middle, which generate some secondary horizontal cracks in the front of the precrack tip if the amplitude of stress waves is large enough. After that, there is a temperature increase in a large region surrounding the cracks (Fig. 10), due to the release of fracture energy. In the case of the loading rate at 100 m/s, the colliding waves cannot generate an amplitude of stress waves that is large enough to cause secondary fracture, so a typical shear fracture and subsequent crack bifurcation can be found. On the other hand, we have also found that the stress distributions of these two cases are distinctly different. In the case of the loading rate at 100 m/s (see Fig. 13(*a*)), a narrow U-shape tensile stress band ahead of the crack tip is formed after the first stress wave collision, and the maximum tensile stress occurs in the direction of some 45 deg with respect to the precrack direction (see Fig. 13(*a*)); whereas in the case of the loading rate at 400 m/s, a large spindle-shaped tensile stress region (see Fig. 13(*b*)) is formed at the same location. The maximum tensile stress also can be found in this region, and the entire region may be fractured due to the high tensile stress. In summary, different loading conditions may produce different stress waves, which lead to different characteristics of thermal–mechanical responses, and hence a different fracture modes at macroscale.

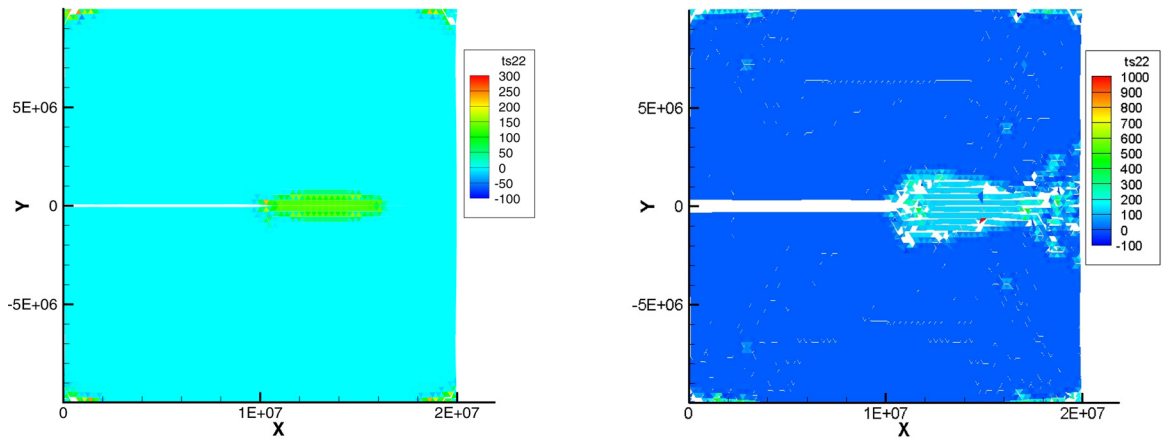

(a) $t = 0.086\mu s$ (b) $t = 0.118\mu s$

Fig. 12 Thermal stress (σ_{22}) distribution at different time (0.83027 × 10^7 Pa) (V_0: 400 m/s, T_0: 293 K)

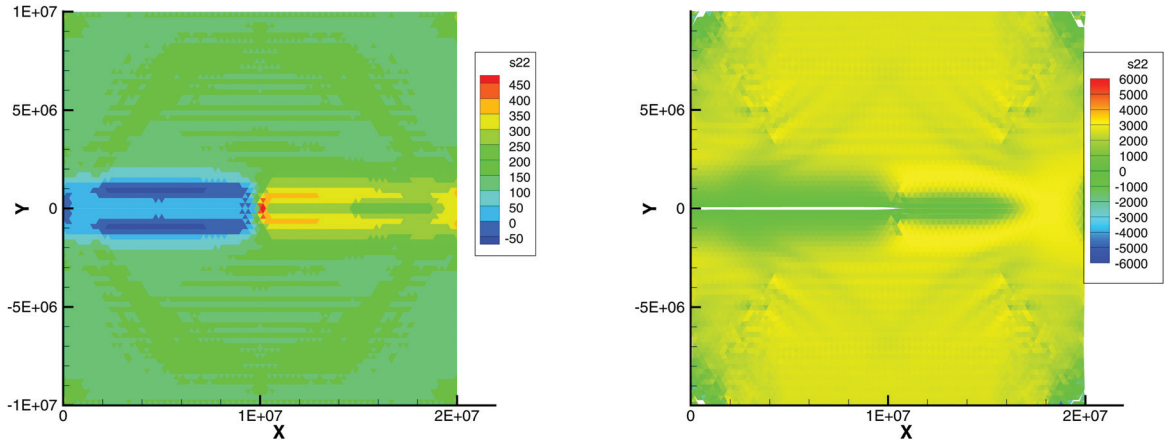

(a) $V_0 = 100m/s$ (b) $V_0 = 400m/s$

Fig. 13 Stress (σ_{22}) distribution at time 0.08 μs (0.83027 × 10^7 Pa) (T_0: 293 K)

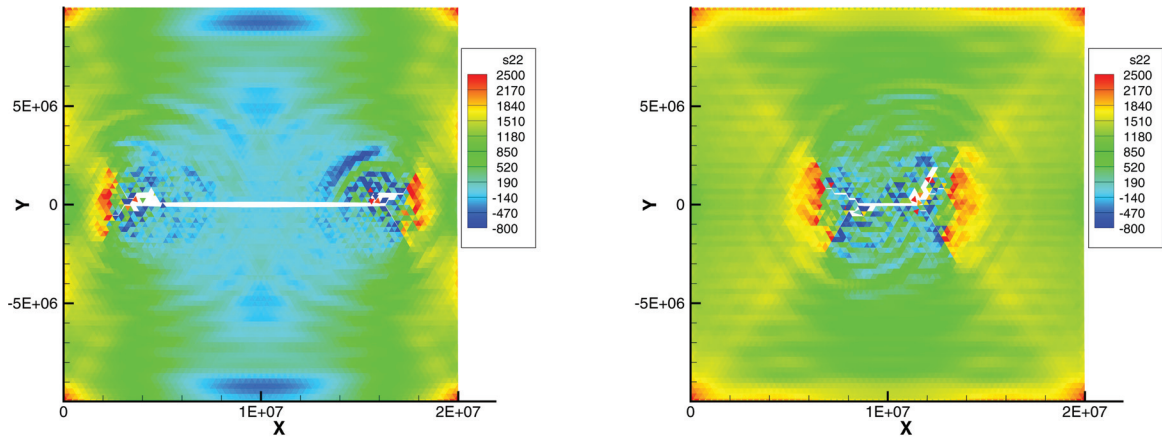

(a) crack length $L = 1mm$ (b) crack length $L = 0.2mm$

Fig. 14 Stress (σ_{22}) distribution at time 0.16 μs for different crack length (0.83027 × 10^7 Pa) (T_0: 293 K, V_0 = 100 m/s)

We also do some preliminary investigation about the size effect of crack length. Figures 14(*a*) and 14(*b*) display the stress distribution for the crack length $L = 1$ mm and $L = 0.2$ mm, respectively. A significant difference of stress distribution for two cases can be found in these figures, in the case of crack length $L = 1$ mm, we can find there is a very large compressive region, but we can't find that in the case of $L = 0.2$ mm. In both two cases, a distinguished tensile region can be found at the head of crack tip, but there only is a slight different for two cases (Fig. 14). The above results indicate our multiscale method can be used to investigate the size effect of crack on the fracture strength of materials, which, as indicated by Gao et al [26], is a main characteristics of small scale fractures.

6 Conclusions

In this work, an atomistic-based thermal–mechanical interphase zone model is proposed, and the associated finite temperature multiscale finite element method has also been implemented. The atomistic-based thermal–mechanical interphase zone model connects the atomistic structure of the material with its macro properties based on statistical thermodynamics. In specific, this is accomplished by combining the Cauchy–Born rule, harmonic approximation, local equilibrium assumption, and colloidal crystal approximation. To make the harmonic approximation and local equilibrium approximation consistent with the Cauchy–Born rule, we postulate at the first time an idealization that is coined as the CLHACC, which makes the multiscale thermal–mechanical finite element possible.

Since the proposed multiscale interphase zone model takes into account thermomechanical coupling effects, we can study the temperature effect on fracture process. In particular, this provides a realistic physical constitutive relation that includes thermal dissipation, which is important in the simulations of material failure and damage during high strain rate loading and high-speed impact, such as spall fracture, propagation of adiabatic shear band, and blast load induced fragmentation. This is because the accurate prediction of thermal dissipation not only provides the correct estimate of energy release rate but also provides a physics-based stable computational formulation that can capture shock wave propagation in solids without invoking artificial damping mechanism to stabilize numerical computations.

Using the finite temperature multiscale finite element method, we have carried out some examples of numerical simulation, and the preliminary results indicate that the proposed method can accurately capture the dynamics fracture process under finite

temperature. For instance, it may be the first time that any simulation result has shown and confirmed that there is a cooling region in front of a moving crack tip.

Acknowledgment

This work was supported by a grant from Army Research Laboratory and a grant from Office of Navy Research (ONR), which are greatly appreciated.

References

[1] Tadmor, E., Ortiz, M., and Phillips, R., 1996, "Quasicontinuum Analysis of Defects in Solids," Philos. Mag. A, **73**(6), pp. 1529–1563.
[2] Gao, H., and Ji, B., 2003, "Modeling Fracture in Nanomaterials Via a Virtual Internal Bond Method," Eng. Fract. Mech., **70**(14), pp. 1777–1791.
[3] Ji, B., and Gao, H., 2004, "Mechanical Properties of Nanostructure of Biological Materials," J. Mech. Phys. Solids, **52**(9), pp. 1963–1990.
[4] Ji, B., and Gao, H., 2004, "A Study of Fracture Mechanisms in Biological Nano-Composites via the Virtual Internal Bond Model," Mater. Sci. Eng., A, **366**(1), pp. 96–103.
[5] Park, H. S., Karpov, E. G., Liu, W. K., and Klein, P. A., 2005, "The Bridging Scale for Two-Dimensional Atomistic/Continuum Coupling," Philos. Mag., **85**(1), pp. 79–113.
[6] Zeng, X., and Li, S., 2010, "A Multiscale Cohesive Zone Model and Simulations of Fractures," Comput. Methods Appl. Mech. Eng., **199**(9-12), pp. 547–556.
[7] Qian, J., and Li, S., 2011, "Application of Multiscale Cohesive Zone Model to Simulate Fracture in Polycrystalline Solids," ASME J. Eng. Mater. Technol., **133**(1), p. 011010.
[8] He, M., and Li, S., 2011, "An Embedded Atom Hyperelastic Constitutive Model and Multiscale Cohesive Finite Element Method," Comput. Mech., **49**, pp. 337–355.
[9] Liu, X., 2006, "Perfectly Matched Multiscale Simulations," Ph.D. thesis, University of California, Berkeley.
[10] Liu, X., and Li, S., 2007, "Nonequilibrium Multiscale Computational Model," J. Chem. Phys., **126**(12), p. 124105.
[11] Yang, W., 2007, "Temperature-Dependent Homogenization Technique and Nanoscale Meshfree Particle Methods," Ph.D. thesis, University of Iowa, Iowa City, IA.
[12] Harris, W. J., 1983, *Statistical Mechanics of Elasticity*, Academic Press, New York.
[13] LeSar, R., Najafabadi, R., and Srolovitz, D. J., 1989, "Finite-Temperature Defect Properties From Free-Energy Minimization," Phys. Rev. Lett., **63**(6), p. 624.
[14] Zhao, R. N. L., and Srolovitz, D., 1993, "Finite Temperature Vacancy Formation Thermodynamics: Local Harmonic and Quasiharmonic Studies," Modell. Simul. Mater. Sci. Eng., **1**(4), pp. 539–551.
[15] Phillpot, S. R., and Rickman, J. M., 1991, "Calculation of the Free Energy of Solids From the Energy Distribution Function," J. Chem. Phys., **94**(2), pp. 1454–1464.
[16] Li, S., and Sheng, N., 2010, "On Multiscale Non-Equilibrium Molecular Dynamics Simulations," Int. J. Numer. Methods Eng., **83**(8-9), pp. 998–1038.
[17] Krishna, P., and Pandey, D., 2001, *Close-Packed Structures*, University College Cardiff Press, Cardiff, United Kingdom.
[18] Schall, P., Cohen, I., Weitz, D., and Spaepen, F., 2005, "Visualizing Dislocation Nucleation by Indenting Colloidal Crystals," Nature, **440**, pp. 319–323.
[19] Suresh, S., 2005, "Colloid Model for Atoms," Nature Mater., **5**, pp. 253–254.
[20] Israelachvili, J., 1992, *Intermolecular and Surface Forces*, Academic, New York.
[21] Li, S., Zeng, X., Ren, B., Zhang, J., He, M., and Jha, A., 2012, "An Atomistic-Based Multiscale Finite Element Method and Simulation of Fracture," Comput. Methods Appl. Mech. Eng, **229-232**, pp. 87–109.
[22] Hattiangadi, A., and Siegmund, T., 2004, "A Thermomechanical Cohesive Zone Model for Bridged Delamination Cracks," J. Mech. Phys. Solids, **52**(3), pp. 533–566.
[23] Houghes, T. J. R., 1987, *The Finite Element Method: Linear Static and Dynamic Finite Element Analysis*, Prentice-Hall, Englewood Cliffs, NJ.
[24] Flores, K. M., and Dauskardt, R. H., 1999, "Local Heating Associated With Crack Tip Plasticity in Zr-Ti-Ni-Cu-Be Bulk Amorphous Metals," J. Mater. Res., pp. 638–643.
[25] Estevez, R., and Basu, S., 2008, "On the Importance of Thermo-Elastic Cooling in the Fracture of Glassy Polymers at High Rates," Int. J. Solids Struct., **45**(11-12), pp. 3449–3465.
[26] Gao, H., Ji, B., Jager, I., Arzt, E., and Fratzl, P., 2003, "Materials Become Insensitive to Flaws at Nanoscale: Lessons From Nature," Proc. Natl. Acad. Sci., **100**(10), pp. 5597–5600.